

# Structure Enhancement Factor Relationships in Single Gold Nanoantennas by Surface-Enhanced Raman Excitation Spectroscopy

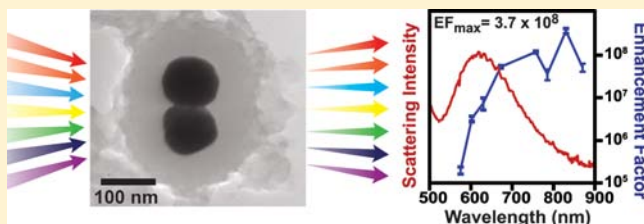
Samuel L. Kleinman,<sup>‡</sup> Bhavya Sharma,<sup>‡</sup> Martin G. Blaber,<sup>‡</sup> Anne-Isabelle Henry,<sup>‡</sup> Nicholas Valley,<sup>‡</sup> R. Griffith Freeman,<sup>§</sup> Michael J. Natan,<sup>§</sup> George C. Schatz,<sup>‡</sup> and Richard P. Van Duyne<sup>\*‡</sup>

<sup>‡</sup>Department of Chemistry, Northwestern University, 2145 Sheridan Road, Evanston, Illinois 60208, United States

<sup>§</sup>Cabot Security Materials Incorporated, 325 East Middlefield Road, Mountain View, California 94043, United States

## S Supporting Information

**ABSTRACT:** Determining the existence of any direct spectral relationship between the far-field scattering properties and the near-field Raman-enhancing properties of surface-enhanced Raman spectroscopy (SERS) substrates has been a challenging task with only a few significant results to date. Here, we prove that hot spot dominated systems show little dependence on the far-field scattering properties because of differences between near- and far-field localized surface plasmon resonance (LSPR) effects as well as excitation of new plasmon modes via a localized emitter. We directly probe the relationship between the near- and far-field light interactions using a correlated LSPR-transmission electron microscopy (TEM) surface-enhanced Raman excitation spectroscopy (SERES) technique. Fourteen individual SERS nanoantennas, Au nanoparticle aggregates ranging from dimers to undecamers, coated in a reporter molecule and encased in a protective silica shell, were excited using eight laser wavelengths. We observed no correlation between the spectral position of the LSPR maxima and the maximum enhancement factor (EF). The single nanoantenna data reveal EFs ranging from  $(2.5 \pm 0.6) \times 10^4$  to  $(4.5 \pm 0.6) \times 10^8$  with maximum enhancement for excitation wavelengths of 785 nm and lower energy. The magnitude of maximum EF was not correlated to the number of cores in the nanoantenna or the spectral position of the LSPR, suggesting a separation between near-field SERS enhancement and far-field Rayleigh scattering. Computational electrodynamics confirms the decoupling of maximum SERS enhancement from the peak of the scattering spectrum. It also points to the importance of a localized emitter for radiating Raman photons to the far-field which, in nonsymmetric systems, allows for the excitation of radiative plasmon modes that are difficult to excite with plane waves. Once these effects are considered, we are able to fully explain the hot spot dominated SERS response of the nanoantennas.



## 1. INTRODUCTION

Surface-enhanced Raman spectroscopy (SERS) is a valuable analytical tool for the ultrasensitive identification and quantification of a host of molecules ranging from chemical warfare agents to biomolecules and artist dyestuffs.<sup>1,2</sup> At the outset, SERS was a niche technique with relatively few applications, namely, monitoring spectroelectrochemical and redox-related reactions<sup>3–5</sup> and elucidating fundamental aspects of surface-mediated spectroscopies.<sup>6,7</sup> Attention persisted in the field through the 1980s and into the next decade, and the seminal claims of observation of SERS signal from a single molecule in 1997<sup>8,9</sup> added interest to the field. The implementation of modern instrumentation for preparing and characterizing substrates and for measuring and interpreting spectra has driven activity to the present day.

Presently, the incorporation of nanoparticles with a strong SERS response is attractive in a wide variety of applications ranging from *in vivo* measurements of cellular processes to pharmaceutical tracking.<sup>10</sup> One very promising and stable material for this application is aggregated nanoparticles encapsulated with silica, commonly known as SERS nanoantennas. The nanoantennas used in this work consist of 90 nm

Au particles functionalized with a reporter molecule then lightly aggregated and subsequently coated with a protective SiO<sub>2</sub> shell. This coating makes them extremely stable, lasting in aqueous solution for years after creation. Additionally, glass particles are largely inert in biological systems, and if needed, the silica can be modified via silane chemical linker protocols.<sup>11,12</sup> The nanoantennas are composed of various numbers of Au cores, ranging from monomers to aggregates exceeding 10 constituents. Nanoantennas are not adversely affected by centrifugation methods; furthermore, centrifugal processing has been implemented to improve the average SERS signal per nanoantenna by removing the less-active monomer components from the resulting synthetic mixture.<sup>13</sup> The reporter molecules are added after nanoparticle synthesis, and the variety of distinct reporter options is extremely diverse. In this case we examine SERS nanoantennas labeled with trans-1,2-bis(4-pyridyl)-ethylene (BPE), a model SERS probe. Nanoantennas are easily integrated into a variety of materials and can provide a stable signal in many conditions. The question remains: What are the

Received: September 19, 2012

Published: December 6, 2012

best and easiest experimental conditions to extract highest enhancement for a given nanoparticle aggregate? And why do these conditions work best from a physics standpoint?

Investigations of ensemble-averaged SERS on lithographically prepared periodic substrates have attempted to characterize the best conditions for SERS given the far-field scattering properties of a substrate. This approach can be valid if the substrate does not contain hot spots, such as the two subsequently discussed. One of the first lithographically prepared SERS substrates was created by the evaporation of Ag onto SiO<sub>2</sub> posts. The localized surface plasmon resonance (LSPR) spectrum of the resulting substrate was not reported, however an excitation profile demonstrated that the SERS enhancement is dependent upon the aspect ratio of the particles.<sup>14</sup> Varying aspect ratio of the plasmonic particles changes the wavelength of the plasmon resonance  $\lambda_{\text{max}}$ .<sup>15</sup> The wavelength-dependent SERS enhancement should arise from tuning the laser frequency into the ensemble plasmon resonance of the Ag particles. A direct demonstration of this effect for an ensemble of nearly identical plasmonic particles was demonstrated in 2005 by McFarland et al.<sup>16</sup> In this work, periodic particle array surfaces prepared by nanosphere lithography were used as a SERS substrate for Raman excitation spectroscopy measurements. The authors discovered that the peak SERS enhancement is obtained when the laser frequency is higher in energy than the plasmon resonance by approximately one-half of the vibrational mode energy. This was rationalized as arising from plasmonic enhancement of both the incoming (exciting) and outgoing (Raman scattered) photons; therefore, the maximum enhancement is obtained with incident laser excitation on the blue side of the plasmon resonance, while the Stokes shifted wavelength is on the red side. The two reports described above provide convincing evidence for a direct relationship between maximum SERS enhancement and the LSPR peak for systems which do not contain hot spots. However, a strikingly different result has been observed while studying single-molecule SERS (SMSERS), where substrates necessarily contain hot spots.

Early SMSERS experiments concentrated on the optical properties of the vibrational signal.<sup>8</sup> Later, Brus and co-workers conducted correlated atomic force microscopy (AFM)-LSPR-SMSERS experiments on Ag colloidal particles. This group observed that the spectral position of the LSPR  $\lambda_{\text{max}}$  of the SMSERS-supporting nanoparticle aggregates was not correlated to the overall SMSERS signal intensity.<sup>17</sup> In a subsequent report, AFM revealed that all SMSERS-supporting Ag colloidal substrates were in fact aggregates of at least two distinct particles.<sup>18</sup> To explain these observations, it has been suggested that a 'hot spot' forms at the junction between particles and controls the SERS response of the particles.

Both experiments and electrodynamic calculations have firmly established the concept of a 'hot spot' in systems with closely interacting plasmonic objects.<sup>19–21</sup> Recently, a few manuscripts have examined the spectral position of the maximum SERS enhancement for a hot spot dominated system.<sup>22</sup> Theoretical modeling has been invoked to demonstrate the differences in regions of high-electromagnetic field enhancement between interfering excitations of single-particle plasmons in a multi-particle system and a collective and phase-coherent excitation of the LSPR. Notably, there is a general trend of increasing SERS enhancement as the excitation energy moves toward the near IR for both Ag<sup>23</sup> and Au<sup>24</sup> dimers based on simulations. In particular, Doherty and co-workers created nearly periodic gold nanorod arrays with a  $\lambda_{\text{max, LSPR}} = 600$  nm using anodic aluminum oxide templates and coated them with either rhodamine 6G or

crystal violet (i.e., resonant Raman) probe molecules. The resulting geometry allows for particles in very close contact and should permit the formation of hot spots.<sup>25</sup> Their results demonstrate that the largest and nearly constant SERS enhancement is observed with excitation energies between 700 and 800 nm and is spectrally distinct from the far-field LSPR resonance of the bulk sample. The manuscript argues that for a hot spot dominated system, the connection between the LSPR maximum and spectral position of maximum SERS enhancement is tenuous at best. This argument is further supported by the work of Itoh et al., who examined Ag nanoparticle aggregates coated with rhodamine 6G at 5 excitation wavelengths ( $\lambda_{\text{ex}} = 458–633$  nm) and found that for the relationship between SERS enhancement, excitation wavelength, and plasmon resonance maxima was somewhat linear.<sup>26</sup> However, the aggregates displayed strong SERS enhancement at wavelengths far from the peak of the plasmon resonance, in support of what is observed in the present manuscript.

Recently, Zuloaga and Nordlander<sup>27</sup> invoked a damped harmonic oscillator model for conduction electrons undergoing plasmonic excitation. This model explained how there can be a red-shift of the peak field enhancement compared to the peak LSPR extinction. In this case, the maximum oscillator displacement occurs at a frequency below the fundamental frequency of the oscillator, with the difference between the frequencies is related to the damping (radiative or otherwise) in the nanostructure. Other mechanisms describing the variation between the near and the far field properties of plasmonic nanostructures were reported by Litz et al.<sup>22</sup> They noted that the resonant modes of individual nanoparticles in an aggregate can interfere, leading to reduced far-field scattering, while maintaining strong local fields.

To provide new insight into the connection between far-field and near-field light-matter interaction, we present correlated measurements involving (1) surface-enhanced Raman excitation spectroscopy (SERES), (2) LSPR, and (3) high-resolution transmission electron microscopy (HRTEM) for individual nanoantennas, along with accurate electromagnetic calculations. Fourteen individual nanoantennas were optically and structurally characterized. There were two dimers and three trimers present in the set of fourteen. The simplest structural model problems—dimers and trimers—are the present focus of the manuscript. The results indicate that the wavelength dependence of the single nanoantennas SERS intensity is dominated by the hot spots created by the interaction of discrete gold cores as well as the excitation of plasmon resonances by the Raman dipole emitter in close proximity to the hot spot.<sup>28</sup> These results show the importance of dipole reradiation effects in the SERS enhancement expression,<sup>19,29</sup> in this case leading to a wavelength of maximum enhancement observed in our SERES experiment for all individual nanoantennas that is sometimes unrelated to the plasmon maximum associated with the single nanoantenna as well as the ensemble LSPR spectrum. This observation is remarkable given the previous literature for discrete nanoantennas.<sup>14,16,30</sup> We will show instead that nanoantenna SERS behavior is dominated by hot spots and the excitation of dark plasmon resonances, which are typically inaccessible by plane wave excitation.

We employed eight distinct Raman laser excitation wavelengths ( $\lambda_{\text{ex}}$ ) between 575 and 870 nm to create the excitation profiles. This window encompasses maxima and minima in the LSPR spectra for a variety of nanoantennas examined. Remarkably, the trend of enhancement factor (EFs) between

individual nanoantennas is qualitatively similar. Close to the gold interband transitions—on the blue edge of our excitation window—the SERS enhancement is relatively low,  $\sim 10^5$ . As the excitation energy is tuned to lower energies, the enhancement increases, and each nanoantenna reaches a maximum EF at some point between  $\lambda_{\text{ex}} = 785$  and 870 nm. This result is in line with the theoretical work of Blaber and Schatz<sup>24</sup> who showed that for dimers of gold nanoparticles with a fixed 1 nm gap, the optimum EF occurs at around 700 nm. In our case, the gap between the spheres varies between samples. As the ratio of nanoparticle diameter to gap between nanoparticles increases, the optimum enhancement red-shifts.

These observations are significant for the rational incorporation of hot spot containing SERS systems into detection and analysis techniques. They are distinct from the commonly accepted, and in some cases correct assumption, that the far-field scattering properties are spectrally related to the position of greatest SERS enhancement. In a hot spot dominated system, the relationship between maximum LSPR and EF is not direct, this theoretical and experimental study will substantiate our claims.

## 2. EXPERIMENTAL SECTION

**2.1. Materials and Methods.** BPE-coated nanoantennas were obtained from Cabot Security Materials, Inc. and used without further purification. Nanoantennas were diluted 1000 $\times$  to achieve a nanoparticle concentration reasonable for drop-casting. Coverslips (Fisher Scientific, no. 1, 25 mm diameter) were thoroughly cleaned with piranha solution, rinsed copiously with Milli-Q water (18.2 M $\Omega$ /cm), subsequently base treated using a 5:1:1 combination of H<sub>2</sub>O:NH<sub>4</sub>OH:H<sub>2</sub>O<sub>2</sub>, and again rinsed copiously with Milli-Q water. BPE (97% Sigma) and methanol (HPLC grade, Sigma) were used without further purification to create solutions ( $\sim 100$  mM BPE) for solution-phase normal Raman characterization.

**2.2. HRTEM.** Support films used were ultrathin carbon type A coated 400 mesh Cu grids obtained from Ted Pella, which have a 30–60 nm thick layer of Formvar (polyvinyl formal) on one side and a 3–4 nm layer of amorphous carbon on the other side. Approximately 5  $\mu$ L of diluted nanoantenna solution was applied on the Formvar side. A JEOL JEM2100 FAST TEM operating at 200 kV was used for all TEM images which were subsequently processed using ImageJ.

**2.3. Optical Microscopy Instrument.** All optical measurements were conducted on an inverted microscope (Nikon, Ti-U) before TEM characterization. Sample motion was accomplished using a nanopositioning stage (Physik Instrumente, model E-500). A 1/3 m spectrograph (Princeton Instruments, SP2300i) dispersed the light using a 150 groove/mm grating for LSPR measurements and a 1200 groove/mm grating for Raman spectroscopy. The dispersed light was collected on a liquid nitrogen cooled CCD (Princeton Instruments, Spec 10).

**2.4. LSPR Instrumentation.** Broadband illumination was provided by a pillar-mounted quartz–tungsten–halogen lamp directed through a dark-field condenser (Nikon, NA = 0.8–0.95). A 100 $\times$  oil-immersion objective, NA set to 0.5, collected Rayleigh scattered light from the nanoparticles, which was then directed to the spectrograph and detected by the CCD camera.

**2.5. Wavelength-Scanned Raman Spectroscopy Instrumentation.** Samples were illuminated by laser excitation from two sources, both with pulse widths on the order of 3 ps. A synchronously pumped, periodically poled, intracavity-doubled optical parametric oscillator (Coherent Mira-OPO, 80 MHz, ps-configuration) was pumped by a mode-locked Ti:Sapphire oscillator at 830 nm (Spectra-Physics Tsunami, 80 MHz, ps-configuration). The OPO provided excitation between 575 and 675 nm. Excitation between 757 and 870 nm was provided by the tunable Ti:Sapphire oscillator. A diode pumped solid-state laser (Spectra-Physics Millennia, 532 nm) was used to drive the oscillator. Both Raman excitation sources were filtered by a grating pinhole spatial filter to narrow the excitation line width. After spectral

filtering, the laser was passed through a half-waveplate followed by a beamsplitter. These two optics served the dual purpose of maintaining a constant input polarization as well as variable power attenuation. The samples were illuminated in an epi configuration such that both excitation and collection of the inelastic Raman scattering were performed with the same objective (Nikon, Plan Fluor 40X) on an inverted microscope. Laser line filtering was accomplished by a combination of long pass filters for convenient wavelengths ( $\lambda_{\text{ex}} = 785$  and 630 nm) as well as tunable bandpass filters (Semrock, VersaChrome) for more exotic excitation wavelengths. Typical powers used for single nanoantenna samples were  $\sim 30$   $\mu$ W to ensure no photodamage occurred throughout the duration of the experiment. Typical powers used for solution-phase measurements were  $\sim 1$  mW which provided adequate signal in a 5–50 s acquisition time. All Raman spectra were frequency calibrated with cyclohexane, providing an absolute Raman shift standard.

**2.6. Computational Modeling.** The scattering properties were calculated using the generalized multiparticle Mie (GMM) method of Xu<sup>31</sup> with extensions by Ringler.<sup>32</sup> In this method, the local fields of the interacting particles are expanded in vector spherical harmonics, and we found it necessary to include vector spherical harmonics up to a minimum degree 40 to ensure convergence.<sup>24</sup> The simulation was performed in a uniform background medium with a refractive index of 1.4, slightly below the refractive index of the silica coating layer (1.55), to account for the air surrounding the nanoantennas. The surface average field enhancement  $\langle E^4 \rangle$  was calculated by averaging the electric field enhancement at 3000 points over the surface of each sphere at each excitation wavelength. The scattering efficiency, absorption efficiency, and surface average field enhancement were then polarization averaged. The line shape of  $\langle E^4 \rangle$  with different polarization angles was qualitatively similar, therefore we present the polarization averaged data. The polarization resolved data for the trimer investigated in Figures 3, 4, and 5 *vide infra* are presented in the Supporting Information (SI). The size and orientation of the simulated structures were derived from TEM images with the exception of the interparticle gap. Here we have used gaps of  $\sim 0.5$  nm in the simulations. At such small length scales, classical electrodynamics begins to break down and nonlocal effects<sup>33,34</sup> reduce the magnitude of the electric field and blue-shift resonances compared to classical theories (as is used here). In the structures considered here, however, there are cases where particles are joined and possess an effective negative gap. McMahon et al. have shown that for touching spheres with an effective negative gap, the resonance position is red-shifted, and the field enhancement increased compared to the positive gap equivalent.<sup>19</sup> We will show that the GMM simulations presented here are in good agreement with experiment due to partial cancellation of these competing effects.

The electronic structure calculations presented in this work have been performed using the Amsterdam Density Functional (ADF) program package.<sup>35</sup> Full geometry optimization and frequency calculations for isolated BPE were completed using the gradient corrected Becke–Perdew (BP86) exchange–correlation functional and a triple- $\zeta$  polarized Slater-type (TZP) basis set. Polarizabilities were calculated using the AORESPONSE module with the same level of theory. Scalar relativistic effects were accounted for with the zeroth-order regular approximation (ZORA).

Raman intensities are calculated by taking derivatives of static polarizabilities with respect to the vibrational normal coordinates. Derivatives are calculated using three-point finite differentiation. Orientational averaging of the molecule with respect to the incident light is assumed leading to a combination of the derivatives as outlined by Yang et al. Intensities are presented as Raman differential cross sections which are related to the polarizability derivatives by eq 1:<sup>36</sup>

$$\frac{d\sigma_p}{d\Omega} = \frac{\pi^2}{\epsilon_0^2} (\omega - \omega_p)^4 \frac{\hbar}{8\pi^2 c \omega_p} [45\bar{\alpha}'_p{}^2 + 7\gamma'_p{}^2] \frac{1}{45(1 - e^{(-\hbar c \omega_p / k_B T)})} \quad (1)$$

where  $\omega$  and  $\omega_p$  are the frequencies of the incident radiation and the  $p^{\text{th}}$  vibrational mode, respectively, and the scattering factor  $45\bar{\alpha}'_p{}^2 + 7\gamma'_p{}^2$  is composed of the isotropic ( $\bar{\alpha}'_p$ ) and anisotropic ( $\gamma'_p$ ) polarizability derivatives with respect to the  $p^{\text{th}}$  vibrational mode.

### 2.7. Calculation of Enhancement Factor and Uncertainties.

Raman spectra of BPE in methanol as well as a neat methanol solution were collected in triplicate at each of the 8 excitation wavelengths. The solvent spectrum was subtracted from each BPE solution spectrum prior to data analysis. Single nanoantenna spectra were also collected in triplicate at each wavelength. All vibrational data were processed using custom software written for MATLAB. Briefly, the data are smoothed, and a linear baseline is established for each peak. Peaks are fit to a Lorentzian line shape, and peak area is integrated, providing a table of integrated peak areas ( $I_{\text{NR}}$  and  $I_{\text{SERS}}$ ) and standard deviations. The following BPE vibrational modes were analyzed: 1008, 1200, 1338, 1604, and 1640  $\text{cm}^{-1}$ . Conversion factors related to instrument response and throughput were removed by utilizing the same laser, microscope, optical filter, and detection system for each excitation wavelength.

The laser spot size was carefully characterized in two dimensions orthogonal to the direction of propagation for both wet and dry samples using the scanning knife edge method.<sup>37</sup> A 25  $\mu\text{m}$  thin Si wafer suspended in methanol or air was the knife which was translated across the beam waist while recording transmitted laser power. These data were fit to an error function with fitting parameters which included the  $1/e^2$  radius of the beam waist. The focal volume was characterized in the direction of laser propagation. The Raman signal from Si was recorded as the sample was translated into and out of the beam waist. Integrated intensity from the 501  $\text{cm}^{-1}$  band of Si was fit to a Gaussian line shape, and the  $1/e^2$  radius determined. From these values it is possible to account for differences in excitation power density ( $P_{\text{ex}}$ ) and number of Raman scatterers ( $N_{\text{NR}}$ ) with respect to spot size and whether the sample was dry or wet. The number of SERS probes ( $N_{\text{SERS}}$ ) per core was estimated to be 14 000 in a previous work using similar samples,<sup>38</sup> hence, 14 000 multiplied by the number of cores in a single nanoantenna, counted from HRTEM images, provided the total  $N_{\text{SERS}}$  that is used to calculate the EF for each nanoantenna using eq 2:

$$\text{EF} = \frac{I_{\text{SERS}}/N_{\text{SERS}}}{I_{\text{NR}}/N_{\text{NR}}} \quad (2)$$

Uncertainty was calculated as the standard deviation of specific mode intensity between the triplicate measurements. This value was then propagated through the EF equation as relative error until being multiplied by the calculated EF, yielding the relative uncertainty in EF for a given wavelength and vibrational mode. Error bars are presented on EF graphs displaying this data and represent one standard deviation above and below the mean.

**2.8. UV–vis Extinction Spectroscopy.** Visible extinction spectroscopy was conducted on a Cary 5000 system. Nanoantennas (40 $\times$  concentration) were diluted  $\sim 50\times$  with Milli-Q water, yielding a peak absorbance of  $\sim 0.45$ . Plastic cuvettes were employed, and the reference solution was deionized water.

## 3. RESULTS AND DISCUSSION

Twenty distinct nanoantennas were identified which provided stable BPE SERS signals. Throughout the course of the experiment a few nanoantennas became inactive, most likely due to photodegradation of the probe molecules. Complete SERES profiles were acquired for 14 nanoantennas at 8 distinct wavelengths. The wavelengths employed were 575.0, 602.1, 630.0, 672.4, 757.0, 785.0, 830.0, and 870.0 nm. Bands at 1008, 1200, 1338, 1604, and 1640  $\text{cm}^{-1}$  were monitored, and the integrated areas were fit by a single Lorentzian function after background fitting and subtraction. All bands displayed the same relative SERES profile shape; therefore, we confine our preliminary discussion to the 1200  $\text{cm}^{-1}$  band.

Figure 1 contains most of the critical information accessible through the correlated SERES-LSPR-TEM process. To our

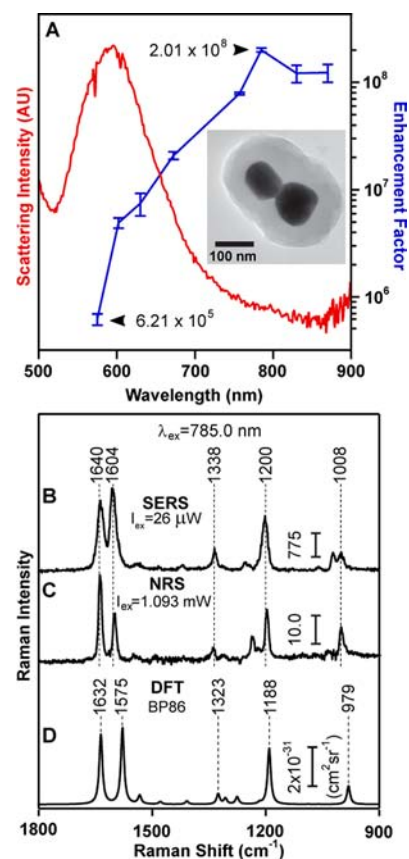


**Figure 1.** Spectral, structural, and theoretical analysis of the nanoantenna dimer inset in panel (A). (A) Scattering spectrum of the nanoantenna in red with the excitation profile for the 1200  $\text{cm}^{-1}$  band in blue. The peak of the excitation profile is spectrally distinct from the peak of the scattering spectrum. (B) SERS spectrum obtained at  $\lambda_{\text{ex}} = 785.0$  nm, the peak of the excitation profile. Comparing the data and signal magnitude in (B) with solution-phase normal Raman spectroscopy in (C) demonstrates the augmentation of Raman signal by the dimer. Vertical scale bars have units  $\text{ADU mw}^{-1} \text{ s}^{-1}$ . (D) Theoretical analysis of the BPE vibrations, a high-fidelity match of peak position and number indicates a thorough understanding of the molecular system; peak frequencies are shifted yet the pattern is reproduced.

knowledge, this is the first correlated analysis of this type on plasmonic nanoparticle aggregates. The dimer of nanospheroids is an archetypical hot spot containing system. Inspection of Figure 1 demonstrates that the maximum enhancement of  $2.01 \times 10^8 \pm 8 \times 10^6$  is obtained when using laser excitation of  $\lambda_{\text{ex}} = 785$  nm. Further to the red, there is slight variation in EFs about  $10^8$ . The lower panel of Figure 1 displays a normal Raman spectrum, SERS spectrum, and DFT simulations of BPE. The peak energies are highly conserved between normal Raman in solution and SERS. There is a weak association between BPE and the Au surface, therefore the vibrational band energies are not changed between techniques, consistent with previous literature precedent.<sup>39</sup> There is a difference in energy between simulations and experiments which varies between 8 and 29  $\text{cm}^{-1}$ . We feel this disparity is largely insignificant and can be attributed to differences between simulations and experiments, including but not limited to: the simulations are calculated for one molecule, whereas experiments measure an ensemble, and also, the simulations are for a gas-phase molecule, whereas experiments are for adsorbed or solvated molecules. The agreement between

techniques demonstrates a thorough understanding of the molecular vibrations of interest in this system.

For this nanoantenna dimer, the LSPR  $\lambda_{\text{max}} = 600$  nm does not coincide with the greatest SERS enhancement. Modeling indicates that there is a separate LSPR maximum at wavelengths above 900 nm, but this is outside the capabilities of the experimental apparatus. Previous experiments on periodic particle arrays, also known as bowtie nanoantenna arrays, would suggest that for a  $1200\text{ cm}^{-1}$  band with a  $\lambda_{\text{max,LSPR}} = 600$  nm, the ideal laser excitation would be  $\sim 580$  nm (the blue-shift noted earlier). This number places the LSPR directly in-between the laser excitation and the emission wavelength for the  $1200\text{ cm}^{-1}$  band.<sup>16</sup> However in a hot spot dominated system, such as the nanoantennas, it is the near-field interaction and amplification of the light which gives rise to SERS.

The hot spot zone has been theorized, calculated, and recently imaged<sup>40</sup> to be a very small region of space directly around the nanoparticle junction. Our results suggest that the hot spot is capable of supporting resonances and amplifying light in the near-field at frequencies that are independent of the scattering  $\lambda_{\text{max}}$ . Additionally, the presence of a localized emitter, which is excited by the Raman process, allows for the excitation of plasmon resonances which are not observable by dark-field microscopy.<sup>28</sup> This contrasts with the Rayleigh scattering behavior, which probes far-field behavior dominated by induced polarization over a much larger spatial region of the dimer. This separation of effects has been recently suggested for other hot spot containing systems,<sup>22,23,25</sup> however we show the first experimental proof of this assertion for single nanoantennas.

Figure 2 shows the nanoantenna which demonstrated one of the highest EFs for any of the 14 nanoaggregates examined. Some larger aggregates provided more signal; however, when normalized for the number of molecules, this nanoantenna provided the strongest enhancement. The structure of the dimer displayed in the inset of Figure 2A appears to be a ‘fused dimer’, similar to those examined in the work of Wustholz et al. In this example, no gap between particles is present, yet the signal magnitude reveals a hot spot is active in the dimer system.<sup>41</sup> The  $\lambda_{\text{max,LSPR}} = 610$  nm, yet the  $\lambda_{\text{max,EF}} = 830$  nm again demonstrating a separation of far-field observables (LSPR) with near-field phenomena (SERS). We calculated the scattering and absorption of a dimer based on the TEM image (Figure 2A, inset) and found that both the scattering and absorbance have local minima around the point of maximum enhancement illustrated in Figure 2B. The blue line in Figure 2B is the polarization averaged, surface averaged enhancement assuming a Stokes shift of zero. The red line in Figure 2B is the polarization averaged scattering cross section, which is deconvoluted in Figure 2C. We now expand the discussion to higher-order aggregates to explore the generality of the observations.

In Figure 3 we present another set of correlated SERES-LSPR-TEM data along with computational modeling for the trimer shown in the inset of panel A. In this specific data set, the agreement between theory and experiment for both scattering and EF is remarkable. The EF attains a maximum value, where the LSPR scattering is relatively low. The highest SERS EF is just above  $10^8$  and is observed for  $\lambda_{\text{ex}} = 785$  and  $830$  nm. The qualitative trend of increasing EF with lower energy excitation is independent of nanoantenna cluster composition, indicating there is an overarching physical phenomenon which governs the response of nanoparticle clusters.

This effect is not limited to only dimers and trimers. In the SI we provide 11 more examples of SERES-LSPR-HRTEM

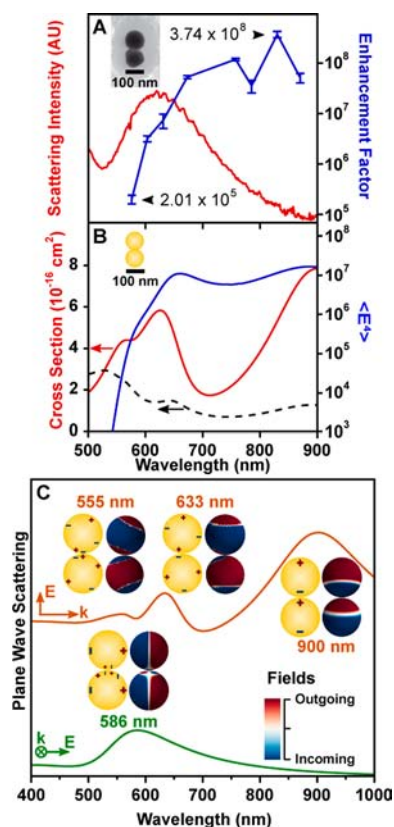


**Figure 2.** Spectral, structural, and theoretical analysis of a nanoantenna dimer with TEM image inset in (A). (A) Scattering spectrum of the nanoantenna in red with the excitation profile for the  $1200\text{ cm}^{-1}$  band in blue. The peak of the excitation profile is spectrally distinct from the peak of the LSPR spectrum. (B) Electromagnetic modeling of the nanoantenna dimer, displaying the  $\langle E^4 \rangle$  enhancement in solid blue, scattering in solid red, and absorbance in black dashed line (B). (C) Results of plane wave scattering for two different polarizations. Charge distributions for specific plasmon resonances are depicted with plus (+) and minus (-) signs as well as color maps of field direction.

measurements of nanoantennas. Although some excitation profiles appear to track the LSPR maximum, we claim this is merely a coincidence. Overall, the excitation profiles demonstrated consistent shape with the lowest enhancement coming from the highest energy excitation and the highest enhancement coming from lower energy Raman excitation. The trend in enhancement is apparently independent of LSPR spectral position. This result has been suggested before, owing to interfering excitations of conduction electrons, generating highly enhanced electromagnetic fields (near-field) without phase coherence of the individual particle plasmons (far-field).<sup>22</sup> The following simulations explain a theoretical basis for strong surface enhancement away from the peak of far-field scattering for the specific nanoantennas studied herein.

The GMM simulations for the nanoantenna trimer presented in (Figure 3A, inset) largely mirror the results in Figure 2B; the polarization-averaged scattering and absorbance spectra are displayed in Figure 3B. There is maximum SERS enhancement in the region where extinction is lowest, with the scattering spectrum being qualitatively similar to that observed experimentally. Differences can be explained based on previous work by McMahon et al., which showed that these structures commonly exhibit LSPR maxima at wavelengths above 900 nm and that the exact wavelength of each resonance is extremely

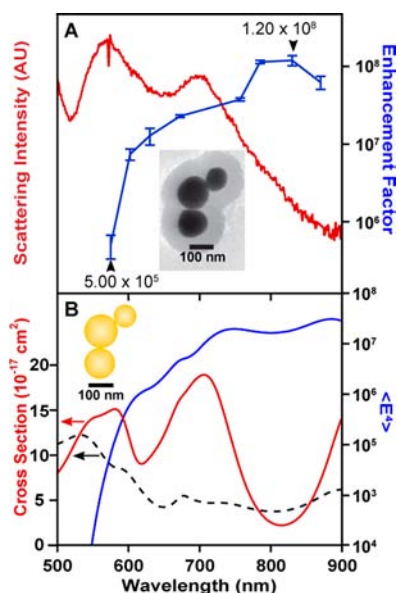


**Figure 3.** Experimental and calculated correlated HRTEM-LSPR-SERES data for the nanoantenna trimer presented in the inset of panel (A). (A) Experimental dark-field scattering spectrum (red) and excitation profile for the  $1200\text{ cm}^{-1}$  band (blue) of the trimer. (B) Electromagnetic modeling of the nanoantenna trimer, displaying the  $\langle E^4 \rangle$  enhancement in solid blue, scattering in solid red, and absorbance in black dashed line (B). Both experimentally and theoretically, the trimer provides maximal SERS enhancement, where the far-field scattering is relatively weak.

sensitive to antenna geometry.<sup>42</sup> In the simulation there are small gaps between the gold nanoparticles which are not evident in the TEM images, so the appearance of a resonance beyond 900 nm (Figure 3B) can be attributed to sub-nanometer variations between the simulated and the experimental structures.

To illustrate the relationship between the near-field properties of the nanoantennas and the far-field LSPR scattering, field profiles of the trimer nanoantenna from Figure 3 are presented in Figure 4. Two wavelengths were chosen to perform the analysis: the scattering maximum at 708 nm and the scattering minimum at 820 nm (Figure 3B). The top panels of Figure 4 depict that the far-field scattering intensity ( $|E|^2$ ) is substantially lower at 820 nm than at 708 nm. This is caused by destructive interference of the multipole contributions to the polarization of the individual spheres when the excitation wavelength is 820 nm. Additionally, there is destructive interference between the +y and -y scattered fields at 820 nm that is not evident at 708 nm. It has been previously demonstrated for SMSERS experiments on Ag colloids that plasmonic enhancement can be caused by interfering plasmon excitations which may not manifest themselves in the scattering spectrum.<sup>22</sup> The bottom panels of Figure 4 show that the surface average field enhancement ( $|E|^4$ ) varies by less than an order of magnitude between 708 and 820 nm. It is interesting to note that  $\lambda_{\text{ex}} = 708\text{ nm}$  causes both junctions to contribute to SERS enhancement, yet at  $\lambda_{\text{ex}} = 820\text{ nm}$  the lower junction contributes most of the enhancement. This result is in line with the results of Litz et al,<sup>22</sup> who showed that phase coherent resonances (like the one shown in Figure 4A,C, where the far field scattering is at a maximum) have the most spatially delocalized near-field enhancement regions. Whereas interference in the 820 nm case (Figure 4B,D) leads to minimal far field scattering, while the near field is still strongly enhanced, albeit more strongly localized in the gap region.<sup>22</sup>

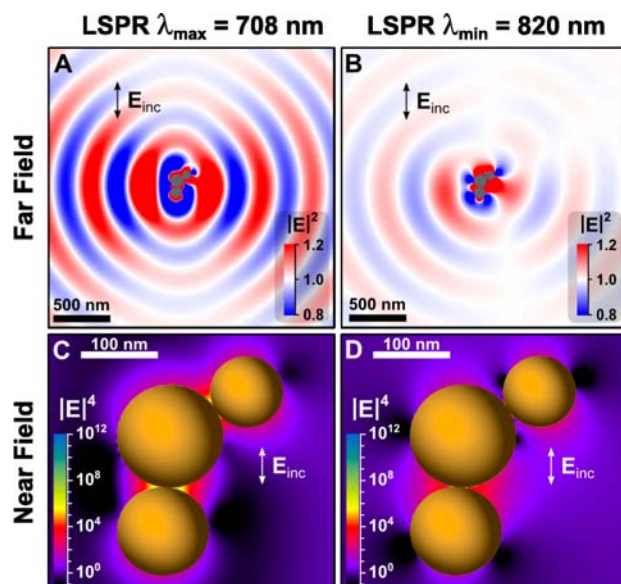


**Figure 4.** Far- (top row) and near-field (bottom row) electromagnetic interactions for peaks and troughs in the LSPR spectrum for the nanoantenna displayed in Figure 3: (A,C)  $\lambda_{\text{ex}} = 708\text{ nm}$  and (B,D)  $\lambda_{\text{ex}} = 820\text{ nm}$ . The lower panels show the large electric field enhancement in the gap region between touching spheres. For both wavelengths the near-field intensity is very similar, manifested in similar EFs. The far-field scattering intensity is smaller at 820 nm than at 708 nm, manifested in different LSPR intensities at the studied wavelengths and illustrated by a difference in the light waves emanating from the particle upon irradiation.

Note however that while Figure 4 graphically illustrates the difference in far-field scattering, it does not contain all of the information regarding how the Stokes-shifted photons are radiated out from the nanostructure so efficiently. To address this point we now consider the dipole reradiation component<sup>29</sup> of the SERS EF.

Plasmon resonance modes which are difficult to excite with far-field excitation are commonly referred to as 'dark modes'.<sup>43</sup> While these modes appear optically inactive in a simple scattering measurement, specific conditions can excite these resonances, and once excited, they can radiate to the far-field and therefore participate in surface-enhanced spectroscopies. Some methods of exciting these resonances are with an electron beam,<sup>44</sup> by energy transfer from nearby optically excited plasmons,<sup>45</sup> or with a localized emitter placed at or very near the nanoparticle surface.<sup>28</sup> In the case of Raman probe molecules, the far-field Raman scattering as measured by the CCD is the result of a multistep process. First, the Raman excitation laser excites surface plasmons on the nanoantennas, which may or may not radiate to the far field, yet result in a very strong near-field enhancement. The near-field excites the molecules to a virtual state which radiates at the Stokes shifted frequency with dipole character. The dipole emitter can then couple to plasmonic modes on the nanoantennas that are difficult to excite with a plane wave but nonetheless radiate to the far-field.

To illustrate this point we present Figure 5 which shows the radiated power of a dipole emitter placed in the 'hot spot' zone, either in between spheres 1 and 2 or 2 and 3.<sup>21</sup> The peak radiated power occurs at 880 nm, similar to the experimentally observed point of maximum SERS EF. Overall this result shows that a localized emitter in either junction will provide a net increase in SERS efficiency at wavelengths that exhibit minimal far-field

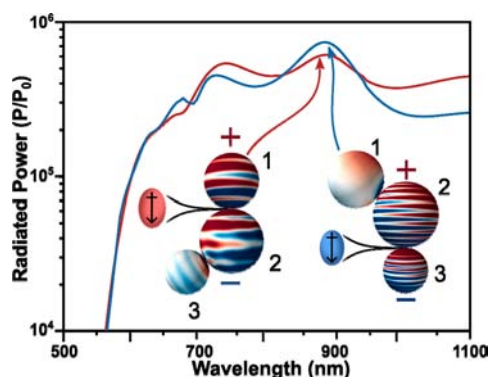


**Figure 5.** Theoretical modeling of nanoantenna trimer examined in Figures 3 and 4. This figure demonstrates the enhancement in radiated power caused by placing a dipole in the crevice between nanoparticles. A peak in the radiated power coincides with the region of maximum SERS enhancement in Figure 3. A dipole within the near-field of the nanoparticles allows for excitation of plasmon resonances, which are difficult to excite with plane wave irradiation.

scattering. This effect acts in conjunction with that illustrated in Figure 4, demonstrating how plasmonic enhancement in the near-field (resulting in SERS) can be separate and distinct from far-field Rayleigh scattering (LSPR). On a single nanoaggregate level, these calculations explain how the greatest SERS enhancement can occur at a different energy than the plasmon resonance of the single nanoantenna. This remarkable result is not isolated to the trimer examined. In fact, it extends to all individual nanoantennas we investigated, we have included the results of a similar calculation for the dimer examined in Figure 2 in the SI. Therefore, the presence of a localized emitter near the nanoparticle intersection also mediates the radiation of photons out of the dimer structure.

The ensemble extinction spectrum for BPE-coated SERS nanoantennas is displayed in Figure 6. The average EF for all

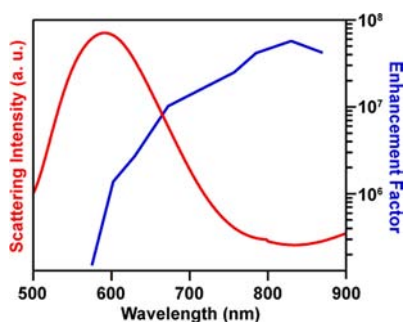


**Figure 6.** The ensemble extinction of a dilute solution of nanoantennas (red trace, left abscissa). The average EF values at 8 wavelengths (blue trace, right abscissa) are presented for all 5 monitored bands for all 14 nanoantennas. Uncertainties are not included as only the general trend is illustrated.

bands monitored at each distinct wavelength with all modes averaged for all 14 nanoantennas is overlaid. It is often suggested that if one measures enough of the parts of a whole (i.e., individual particle attributes), then it is possible to recreate the ensemble measurement. While data from 14 nanoantennas is not a statistically significant sampling, it is important to note that the ensemble LSPR and average EF show different spectral maxima, in agreement with the single particle data sets which are presented earlier. We have chosen to include data from all 14

nanoantennas in Figure 6 to recreate the ensemble-averaged extinction measurement which included all morphologies and sizes of nanoantennas. Additionally, we have provided significant theoretical reconciliation to explain the observed effect. In the visible-near IR extinction spectrum of the nanoantennas there is another extinction maximum about 1000 nm. This spectral region is outside the capabilities of our current experimental setup, yet simulations predict even greater EFs at these wavelengths.<sup>19</sup>

## 4. CONCLUSIONS

In this manuscript we have explored SERES profiles for a number of nanoantenna geometries and sizes. Structural and optical characterization was accomplished by a correlated SERES-LSPR-HRTEM technique. The average EF for individual nanoantennas peaked at  $\lambda_{\text{ex}} = 830$  nm with a value of  $5 \times 10^7$ . Minimum average EFs were recorded with  $\lambda_{\text{ex}} = 575$  nm and are just above  $10^5$ . We found that there is no consistent correlation between the spectral positions of SERS EFs and the LSPR. There was not a significant change in EF based on structure (i.e., number of cores) and all nanoantennas scattered efficiently using  $\lambda_{\text{ex}} = 785$  nm, a commonly available laser line. The maximum EF obtained for a single particle was  $\sim 5 \times 10^8$ . The observed maximum EF is likely not a global maximum as increases in signal can be accomplished by optimizing both laser polarization and particle orientation.

Computational modeling was used to confirm our hypothesis; for a hot spot dominated system, such as aggregated colloidal nanoparticles, the enhancing properties do not follow the spectral properties of the LSPR. From a single nanoantenna, ensemble, and computational perspective the laser frequency which gives the maximum SERS enhancement is not correlated to the peak LSPR frequency. The excitation of new plasmon resonances by the emitting properties (dipole reradiation) of a probe molecule at or near the nanoantenna surface must be considered for aggregates consisting of more than two particles, as this allows for the excitation of 'dark' modes. This set of measurements demonstrates that there is no relationship between the far-field scattering spectrum of a hot spot containing structure and its SERS wavelength response. We ascribe this apparent discrepancy to a separation between near-field effects, observable by SERS, and far-field effects, observable by dark-field scattering.

## ■ ASSOCIATED CONTENT

### 📄 Supporting Information

Plots of EF and dark-field scattering spectrum for 11 more individual nanoantennas. Additionally, a plot demonstrating the radiative power of a dipole in the crevice of the dimer in Figure 2 and the polarization angle-resolved  $\langle E^4 \rangle$  plot of the trimer from Figures 3, 4, and 5. This material is available free of charge via the Internet at <http://pubs.acs.org>

## ■ AUTHOR INFORMATION

### Corresponding Author

vanduyne@northwestern.edu

### Notes

The authors declare no competing financial interest.

## ■ ACKNOWLEDGMENTS

This work was supported by the National Science Foundation (NSF CHE-0802913, CHE-0911145, CHE-1152547, DMR-

1121262) and by DARPA under SSC Pacific grant N660001-11-1-4179. Any opinions, findings, and conclusions or recommendations expressed in this publication are those of the author(s) and do not necessarily reflect the views of DARPA. We acknowledge Semrock Inc. for the generous donation of VersaChrome tunable bandpass filters. Computational time was provided by the Quest High-Performance Computing facility at Northwestern University, which is jointly supported by the Office of the Provost, the Office for Research, and Northwestern University Information Technology. This work made use of the EPIC facility (NUANCE Center, Northwestern University), which has received support from the MRSEC program (NSF DMR-0520513) at the Materials Research Center, Nanoscale Science and Engineering Center (EEC-0118025/003), both programs of the National Science Foundation, the State of Illinois, and Northwestern University.

## REFERENCES

- (1) Wustholz, K. L.; Brosseau, C. L.; Casadio, F.; Van Duyne, R. P. *Phys. Chem. Chem. Phys.* **2009**, *11*, 7350–7359.
- (2) Stuart, D. A.; Yuen, J. M.; Shah, N.; Lyandres, O.; Yonzon, C. R.; Glucksberg, M. R.; Walsh, J. T.; Van Duyne, R. P. *Anal. Chem.* **2006**, *78*, 7211–7215.
- (3) Van Duyne, R. P.; Cape, T. W.; Suchanski, M. R.; Siedle, A. R. *J. Phys. Chem.* **1986**, *90*, 739–743.
- (4) Van Duyne, R. P.; Haushalter, J. P. *J. Phys. Chem.* **1984**, *88*, 2446–2451.
- (5) Van Duyne, R. P. *J. Phys. Colloques* **1977**, *38*, 239–252.
- (6) Moskovits, M. *J. Chem. Phys.* **1982**, *77*, 4408–4416.
- (7) Moskovits, M.; DiLella, D. P.; Maynard, K. J. *Langmuir* **1988**, *4*, 67–76.
- (8) Nie, S.; Emory, S. R. *Science* **1997**, *275*, 1102–1106.
- (9) Kneipp, K.; Wang, Y.; Kneipp, H.; Perelman, L. T.; Itzkan, I.; Dasari, R. R.; Feld, M. S. *Phys. Rev. Lett.* **1997**, *78*, 1667–1670.
- (10) Zavaleta, C. L.; Smith, B. R.; Walton, I.; Doering, W.; Davis, G.; Shojaei, B.; Natan, M. J.; Gambhir, S. S. *Proc. Natl. Acad. Sci. U.S.A.* **2009**, *106*, 13511–13516.
- (11) Slowing, I. I.; Trewyn, B. G.; Giri, S.; Lin, V. S. Y. *Adv. Funct. Mater.* **2007**, *17*, 1225–1236.
- (12) Lin, Y.-S.; Abadeer, N.; Hurley, K. R.; Haynes, C. L. *J. Am. Chem. Soc.* **2012**, *133*, 20444–20457.
- (13) Tyler, T. P.; Henry, A.-I.; Van Duyne, R. P.; Hersam, M. C. *J. Phys. Chem. Lett.* **2011**, *2*, 218–222.
- (14) Liao, P. F.; Bergman, J. G.; Chemla, D. S.; Wokaun, A.; Melngailis, J.; Hawryluk, A. M.; Economou, N. P. *Chem. Phys. Lett.* **1981**, *82*, 355–359.
- (15) Willets, K. A.; Van Duyne, R. P. *Annu. Rev. Phys. Chem.* **2007**, *58*, 267–297.
- (16) McFarland, A. D.; Young, M. A.; Dieringer, J. A.; Van Duyne, R. P. *J. Phys. Chem. B* **2005**, *109*, 11279–11285.
- (17) Michaels, A. M.; Nirmal, M.; Brus, L. E. *J. Am. Chem. Soc.* **1999**, *121*, 9932–9939.
- (18) Michaels, A. M.; Jiang, Brus, L. *J. Phys. Chem. B* **2000**, *104*, 11965–11971.
- (19) McMahan, J. M.; Li, S.; Ausman, L. K.; Schatz, G. C. *J. Phys. Chem. C* **2012**, *116*, 1627–1637.
- (20) Stranahan, S. M.; Willets, K. A. *Nano Lett.* **2010**, *10*, 3777–3784.
- (21) Camden, J. P.; Dieringer, J. A.; Wang, Y.; Masiello, D. J.; Marks, L. D.; Schatz, G. C.; Van Duyne, R. P. *J. Am. Chem. Soc.* **2008**, *130*, 12616–12617.
- (22) Litz, J. P.; Camden, J. P.; Masiello, D. J. *J. Phys. Chem. Lett.* **2011**, *2*, 1695–1700.
- (23) Le Ru, E. C.; Galloway, C.; Etchegoin, P. G. *Phys. Chem. Chem. Phys.* **2006**, *8*, 3083–3087.
- (24) Blaber, M. G.; Schatz, G. C. *Chem. Commun.* **2011**, *47*, 3769–3771.
- (25) Doherty, M. D.; Murphy, A.; McPhillips, J.; Pollard, R. J.; Dawson, P. *J. Phys. Chem. C* **2010**, *114*, 19913–19919.
- (26) Itoh, T.; Kikkawa, Y.; Yoshida, K.; Hashimoto, K.; Biju, V.; Ishikawa, M.; Ozaki, Y. *J. Photochem. Photobiol., A* **2006**, *183*, 322–328.
- (27) Zuloaga, J.; Nordlander, P. *Nano Lett.* **2011**, *11*, 1280–1283.
- (28) Liu, M.; Lee, T.-W.; Gray, S. K.; Guyot-Sionnest, P.; Pelton, M. *Phys. Rev. Lett.* **2009**, *102*, 107401.
- (29) Ausman, L. K.; Schatz, G. C. *J. Chem. Phys.* **2009**, *131*, 084708–10.
- (30) Weitz, D. A.; Garoff, S.; Gramila, T. J. *Opt. Lett.* **1982**, *7*, 168–170.
- (31) Xu, Y.-l. *Appl. Opt.* **1995**, *34*, 4573–4588.
- (32) Ringler, M.; Schwemer, A.; Wunderlich, M.; Nichtl, A.; Kürzinger, K.; Klar, T. A.; Feldmann, J. *Phys. Rev. Lett.* **2008**, *100*, 203002.
- (33) McMahan, J. M.; Gray, S. K.; Schatz, G. C. *Phys. Rev. Lett.* **2009**, *103*, 097403.
- (34) García de Abajo, F. J. *J. Phys. Chem. C* **2008**, *112*, 17983–17987.
- (35) Baerends, E. J., et al. *Amsterdam Density Functional*, 2008.01; SCM: Amsterdam, 2009.
- (36) Neugebauer, J.; Hess, B. A. *J. Chem. Phys.* **2003**, *118*, 7215–7225.
- (37) Bilger, H. R.; Habib, T. *Appl. Opt.* **1985**, *24*, 686–690.
- (38) Wustholz, K. L.; Henry, A. I.; McMahan, J. M.; Freeman, R. G.; Valley, N.; Piotti, M. E.; Natan, M. J.; Schatz, G. C.; Van Duyne, R. P. *J. Am. Chem. Soc.* **2010**, *132*, 10903–10910.
- (39) Yang, W.-h.; Hulteen, J.; Schatz, G. C.; Van Duyne, R. P. *J. Chem. Phys.* **1996**, *104*, 4313–4323.
- (40) Weber, M. L.; Litz, J. P.; Masiello, D. J.; Willets, K. A. *ACS Nano* **2012**, *6*, 1839–1848.
- (41) Wustholz, K. L.; Henry, A. I.; McMahan, J. M.; Freeman, R. G.; Valley, N.; Piotti, M. E.; Natan, M. J.; Schatz, G. C.; Van Duyne, R. P. *J. Am. Chem. Soc.* **2010**, *132*, 10903–10910.
- (42) McMahan, J.; Henry, A.-I.; Wustholz, K.; Natan, M.; Freeman, R.; Van Duyne, R.; Schatz, G. *Anal. Bioanal. Chem.* **2009**, *394*, 1819–1825.
- (43) Nordlander, P.; Oubre, C.; Prodan, E.; Li, K.; Stockman, M. I. *Nano Lett.* **2004**, *4*, 899–903.
- (44) Chu, M.-W.; Myroshnychenko, V.; Chen, C. H.; Deng, J.-P.; Mou, C.-Y.; Garcia de Abajo, F. J. *Nano Lett.* **2008**, *9*, 399–404.
- (45) Lassiter, J. B.; Sobhani, H.; Knight, M. W.; Mielczarek, W. S.; Nordlander, P.; Halas, N. J. *Nano Lett.* **2012**, *12*, 1058–1062.